# Study of morphology, magnetic properties, and visible magnetic circular dichroism of Ni nanoparticles synthesized in $SiO_2$ by ion implantation

I. S. Edelman,[1] D. A. Petrov,[1] R. D. Ivantsov,[1] S. M. Zharkov,[1,2] D. A. Velikanov,[1,2] G. G. Gumarov,[3] V. I. Nuzhdin,[3] V. F. Valeev,[3] and A. L. Stepanov[3,4]

[1]*Kirensky Institute of Physics, Siberian Branch, Russian Academy of Sciences, Akademgorodok, Krasnoyarsk 660036, Russian Federation*

[2]*Siberian Federal University, Svobodnyi pr. 79, Krasnoyarsk 660041, Russian Federation*

[3]*Zavoisky Physical Technical Institute, Russian Academy of Sciences, Kazan 420029, Russian Federation*

[4]*Kazan Federal University, Kazan 420000, Russian Federation*

(Received 18 January 2013; published 29 March 2013)

A systematic study of ensembles of nickel nanoparticles fabricated by $Ni^+$-ion implantation at a dose of $(0.5–1.0) \times 10^{17}$ ions/cm$^2$ in a thin near-surface layer of an amorphous $SiO_2$ matrix by means of transmission electron microscopy (TEM), dc magnetic measurements, and magneto-optical technique is presented. TEM characterization of Ni nanoparticles proves the formation of isolated spherical nickel nanoparticles with diameters from 2 to 16 nm. The crystal structure and lattice constant of the nanoparticles correspond to face-centered-cubic Ni. The larger size nanoparticles are shown to have core-shell structure, which is unusual for the implantation conditions used. The shell of these nanoparticles consists of Ni, while the core has supposedly the composition coinciding with the matrix, i.e., $SiO_2$. The core-shell nanoparticles in the investigated sample coexist with ordinary pure Ni nanoparticles, which strongly affects the magnetic and especially magneto-optic properties of the samples. For all three doses, the nanoparticles are in the superparamagnetic state at room temperature passing to the "frozen" state at lower temperatures. However, only the sample implanted with the lowest dose demonstrates the classic superparamagnetic behavior according to the shape of the experimental magnetization temperature dependencies for the zero-field-cooled (ZFC) and field-cooled regimes. This shape deviation from that characteristic of the pure superparamagnetic ensembles is ascribed mainly to the particle core-shell structure. The Ni nanoparticles' anisotropy constant estimated with the help of ZFC curves appears to exceed the bulk Ni anisotropy second constant approximately by two orders of magnitude. Magnetic circular dichroism (MCD) is characterized by spectral dependence modified strongly as compared to the MCD spectra of a continuous Ni film. In the spectral range 1.1–4.2 eV, the MCD spectrum consists of two broad maxima of opposite sign with the characteristics depending on the implantation dose and the measurement temperature. The MCD spectra analysis allows one to show that the higher-energy maximum (at 3.34–3.48 eV depending on the dose) is related to the surface plasmon resonance (SPR) excitation in pure Ni nanoparticles, while the lower-energy maximum (at 2.19–2.73 eV depending on the dose) should be associated with the SPR excitation in core-shell nanoparticles.

DOI: 10.1103/PhysRevB.87.115435 PACS number(s): 75.75.Fk, 75.75.Cd, 73.20.Mf, 78.20.Ls

## I. INTRODUCTION

Nowadays, the formation of magnetic metal nanoparticles in ionic matrices and glasses is an area of very active research (e.g., Refs. 1–4) driven by a great number of new effects found in nanoscale magnetic systems[5–7] and their technical importance.[8] Ion implantation is a prospective technology to fabricate new materials with nanoparticles and to change effectively the surface properties of a sample.[9] The history of the ion implantation technique application for the synthesis of metal nanoparticles in dielectrics dates back to 1973, when Davenas with coauthors pioneered this method to create small particles of various metals in LiF and MgO ionic crystals.[10] Since then, it has been widely used for the formation of nanoparticles, mainly noble metals in dielectric matrices, in order to obtain new composite materials for the magnetic recording industry and the creation of high-speed optical devices with record high values of nonlinear optical parameters.[11–16] This method allows creating materials that combine the magnetic properties and transparency in the visible spectrum, which may be of interest not only for magnetic recording and nonlinear optics, but also for new combined magneto-optical materials. From the last point of view, magneto-optical properties of ensembles of magnetic nanoparticles attract considerable attention.

One of the interesting aspects of these investigations is associated also with the possibility of the surface plasmon oscillations in small metal nanoparticles and their effect in magneto-optical properties, in particular, for Ni particles.[17] Up to now, the main efforts of the implanted Ni nanoparticles' investigations have been concentrated on the magneto-optical Kerr effect[18,19] (KE). The application of magneto-optical effects in the transmitted light [Faraday rotation and magnetic circular dichroism (FR and MCD, correspondingly)] for such types of Ni nanostructure systems is now at the initial stage. To evaluate the magneto-optical efficiency of a nanomaterial, knowing its behavior in an external magnetic field as well as the magnetic nanoparticles' morphology is also of importance.

Based on the above statements, we devoted the study to morphology, magnetic, and magneto-optical properties of ensembles of Ni nanoparticles fabricated in the $SiO_2$ matrix by low-energy $Ni^+$-ion implantation. Much attention is given to MCD, one of the most powerful magneto-optical effects[20] that has not been investigated earlier for such systems with Ni nanoparticles.

The paper is organized as follows. In Sec. II, the description of the sample preparation and experimental techniques is given. In Sec. III, experimental TEM data are presented and

 

discussed. Section IV deals with the measured temperature and magnetic field dependencies of the static magnetization. In Sec. V, attention is focused on MCD spectroscopic studies of the samples implanted with different doses.

## II. EXPERIMENT

The samples were prepared by implanting fused silica glass plates with $0.5 \times 10^{17}$, $0.75 \times 10^{17}$, and $1 \times 10^{17}$ $Ni^+/cm^2$ (samples D1, D2, D3, respectively) at 40 keV using an ILU-3 ion-beam accelerator in vacuum of $10^{-5}$ Torr.[15,21] A sample holder was cooled by flowing water and the current density was maintained at lower than 8 $\mu A/cm^2$ in order to avoid heating of the sample during the implantation process.

The magnetization temperature and field dependencies were studied with the Quantum Design Magnetic Property Measurement System MPMS XL in the temperature interval 5–300 K. The magnetic field up to 2 T was directed parallel to the sample plane.

Electron-microscopy studies were conducted at the Electron Microscopy Laboratory of the Joint Center of Siberian Federal University using a JEOL JEM-2100 ($LaB_6$) transmission electron microscope (TEM) operating at 200 keV and equipped with an energy dispersive x-ray spectrometer Oxford Instruments INCA x-sight. Selected-area electron diffraction (SAED) was used to determine the lattice structure and the lattice constant of the nanoparticles. Cross-section specimens for TEM were prepared by cutting thin slices of the implanted samples, gluing them face to face with an epoxy resin, and then using conventional methods involving grinding and polishing the samples to a thickness of 10–15 $\mu$m. Finally, $Ar^+$-ion milling was used at an incident ion angle of 6° from both sides of the specimen to make it electron transparent using a Gatan PIPS Model 691 at an operating voltage of 5 keV.

MCD and FR were measured in the normal geometry: the magnetic vector and the light beam were directed normal to the sample plane. The azimuthal modulation of the polarization plane orientation of the incident light wave was used for the FR measurement. The FR angle $\alpha_F$ was measured in the spectral range 1.2–3.8 eV in magnetic field changing from $-0.3$ to 0.3 T with an accuracy of $\pm 0.2$ min. The modulation of the state of the light wave polarization from the right-hand to the left-hand circular polarization was used for MCD measurement. The modulator was made of a fused silica prism with a glued piezoelectric ceramics element. The prism is of $100 \times 15 \times 10$ $mm^3$ in size with horizontal long axis. In the absence of an acoustic excitation, the prism is optically isotropic. When the ac voltage of frequency $\omega$ corresponding to the eigenfrequency of the system is supplied to the piezoelectric ceramics, an elastic standing wave will be excited in the quartz prism. Linearly polarized light with the polarization plane turned to an angle of 45° relatively the horizontal prism axis falls on the prism. At the exit of the prism, the light wave will acquire circular polarization when a standing acoustic wave is excited in it. This polarization changes from the right- to the left-hand circle during one period of acoustic vibration of the prism. In the case of a sample possessing MCD, its absorption coefficients are different for the right- and left-hand circular polarized light waves with respect to the magnetic moment direction of a sample. As a result, the light flux having passed through the sample and reaching a photomultiplier has a modulated intensity. The MCD value was measured as the difference between the photomultiplier voltages for two opposite directions of an applied magnetic field in the spectral range 1.1–4.2 eV in a magnetic field of up to 0.35 T in the temperature range 95–300 K. The measurement accuracy was about $10^{-4}$, and the spectral resolution was 20–50 $cm^{-1}$ depending on the wavelength.

FR of the $SiO_2$ matrix was taken into account: the FR value of Ni nanoparticles was determined as a difference between the spectra recorded for the $Ni^+$-irradiated sample and the initial $SiO_2$ matrix. The measured MCD spectra, according to their definition, are due to magnetic particles only; the transparent substrate does not contribute to this effect.

## III. SAMPLES MORPHOLOGY

Transmission electron microscopy was performed on the ion-implanted samples. The cross-section bright-field TEM images of the samples D2 and D3 (Fig. 1) show isolated nickel nanoparticles with diameters from 2 to 16 nm. The image magnification allows seeing distinctly the core-shell morphology of the nanoparticles [Fig. 1(b)]. The dark-field TEM image [Fig. 2(b)] evidences that all crystalline Ni amounts are concentrated in the shell area of the nanoparticles. Hence, in this case, one can determine them as the "hollow" Ni nanoparticles, keeping in mind nanovoids consisting of the matrix material ($SiO_2$) and containing no crystalline Ni. The shape of the particles (both shells and voids) is seen to be close to a spherical one, which is confirmed by the preservation of the particles' sphericity when the samples are tilted at different angles (up to $\pm 30°$) relative to the electron beam propagation direction.

The elemental composition determined by energy dispersive x-ray spectroscopy supports the presence of nickel in the irradiated layer and its absence outside the implantation modified region. The total thickness of the modified region in $SiO_2$ is about $65 \pm 5$ nm. The set of diffraction reflections in the selected-area electron diffraction pattern [Fig. 2(a)] obtained from the area containing nanoparticles corresponds to the face-centered-cubic (fcc) structure (space group $Fm\text{-}3m$) with a lattice constant: $a = 3.52 \pm 0.01$ Å, which is characteristic of the equilibrium phase of bulk Ni [PDF 4+, card #00-004-0850]. The nickel nanoparticles are located at a depth of 10–15 nm under the sample surface in a thin layer of 30–35 nm thick in sample D2, and at a depth of 5–10 nm

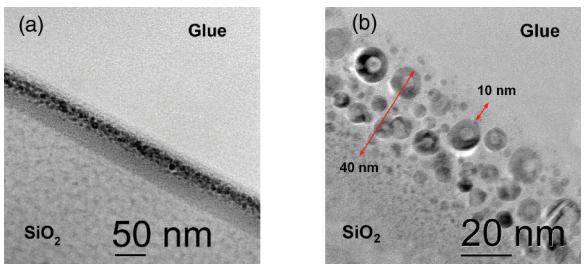


FIG. 1. (Color online) Bright-field TEM images of the cross sections of the samples: D2 (a) and D3 (b).

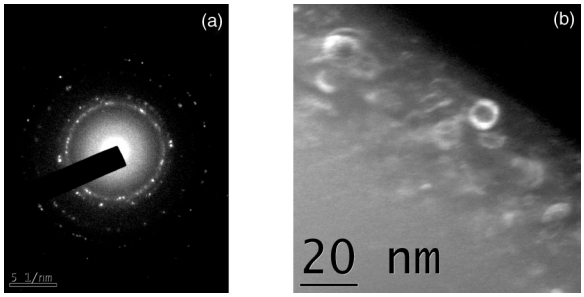


FIG. 2. SAED pattern (a) and dark-field TEM image (b) of the sample D3.

under the sample surface in a thin layer of 35–40 nm thick in sample D3 (Fig. 1).

The core-shell morphology of metal nanoparticles fabricated with the ion implantation technique was observed by several authors.[22–25] In particular, core-shell nanoparticles were demonstrated in Ref. 22 when studying Fe-Al/$SiO_2$ granular solids: the same doses of Fe and Al ions ($1.5 \times 10^{17}/cm^2$) were sequentially implanted at room temperature into fused silica, at energies of 110 keV for Fe and 50 keV for Al. By implanting first the Al ions and later Fe ions, 5–40 nm core-shell crystalline nanoparticles were formed with the lattice parameter corresponding to that of the $\alpha$-Fe. By changing the implantation order, 10–15 nm core-shell nanoparticles of a body-centered-cubic (bcc) Fe-based phase with a lattice 2.5% smaller than that of $\alpha$-Fe were formed. More than that, in the Al-Fe samples, the core-shell nanoparticles had several cores, while in the Fe-Al one there were single-core clusters. It is worth noting that usually such particle morphology is associated with the sequential implantation of two different metals: Fe and Al as in Ref. 22, Ag and Cd as in Ref. 23, Pd and Cu, Pd and Ag, Pd and Fe as in Ref. 24, or Cu and Ag as in Ref. 25. Some authors compared nanoparticle morphology for one-step and two-step implantation processes and noted that in the case of the single-element implantation, the spherical homogeneous nanoparticles were formed in the silica-implanted area.[20] On the other hand, particles containing nanovoids were observed in the silica samples implanted with large doses of the high-energy (200 keV) $Ag^+$ ions.[26] Moreover, high-energy ions were used also by most of the authors when samples with two different metals were implanted.

The origin of core-shell or hollow nanoparticle formation is questionable now. The mechanism is considered more frequently[25,26] and is associated with the high-density vacancies' formation when the initially formed nanoparticles were irradiated by subsequently implanted ions, knocking out atoms from the particles. The vacancies can aggregate into nanovoids driven by the heat produced by the collision cascades. A study is in progress to investigate the mechanisms of the core-shell nanoparticles' formation in silicon substrate implanted with low-energy and low-dose $Ni^+$ ions.

The particles' diameter distribution histograms are shown in Fig. 3 for samples D2 and D3. The histograms were determined from several bright-field TEM images over a total number of 137 and 251 particles for samples D2 and D3, correspondingly. The histograms were fitted using a log-normal distribution of the particle diameter:

$$f(D) = (2\pi\sigma^2)^{-\frac{1}{2}} \frac{1}{D} \exp\left(-\frac{ln^2\left(\frac{D}{\langle D\rangle}\right)}{2\sigma^2}\right). \quad (1)$$

From (1), we obtained the median particle diameter $\langle D\rangle$ to be equal to 6.7 and 7.8 nm ($6.7 \times 10^{-7}$ and $7.8 \times 10^{-7}$ cm) for the samples D2 and D3, correspondingly. The corresponding particle median volumes $\langle V\rangle = \frac{\pi}{6}\langle D\rangle^3 e^{9\sigma^2}$ are $5.6 \times 10^{-19}$ and $9.5 \times 10^{-19}$ $cm^3$ for these two samples, respectively. The nanoparticles' core- and outer-shell diameter distributions are also shown together with the log-normal outer-shell diameter distribution. Note that the larger particles only contain "hollows" while the smaller particles are solid. The count of the solid particles exceeds the count of the core-shell particles; the mean size of the core-shell particles exceeds the mean size of the solid particles. For this reason, the size distribution curves are different for the whole set of particles [green (light gray) solid lines in Fig. 3] and the core-shell particles [red (gray) solid lines in Fig. 3]. For both samples D2 and D3, the maximal number of the core-shell particles has the same core diameter 3 nm. It is possible that it is due to the implantation energy.

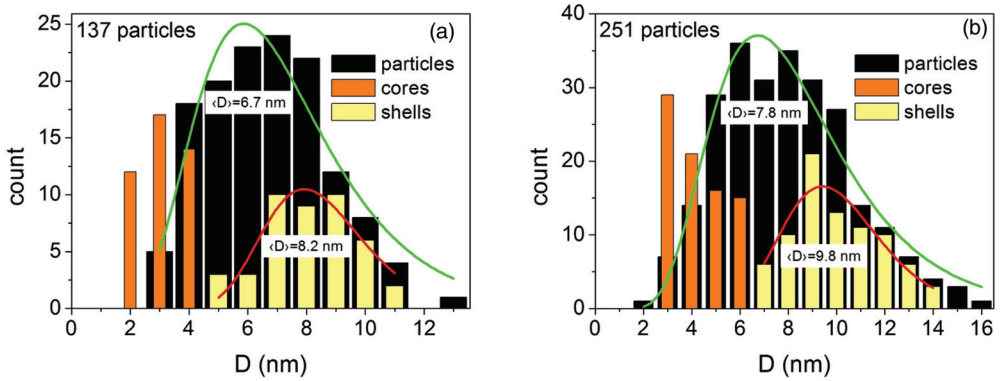


FIG. 3. (Color online) Histograms of diameter distribution: of all nanoparticles, both solid and core shell (black bars); cores [orange (gray) bars] and core-shell nanoparticles [yellow (light gray) bars] for the samples D2 (a) and D3 (b) obtained from the TEM images and adjusted by log-normal curves for the nanoparticles [green (light gray) solid lines] and outer-shell surfaces [red (gray) solid lines].

## IV. MAGNETIZATION FIELD AND TEMPERATURE DEPENDENCIES

Previously, using ferromagnetic resonance (FMR), we have shown that the samples implanted with nickel have easy-plane anisotropy,[27] which is typical for many planar ensembles of magnetic nanoparticles that are observed experimentally with different techniques and considered theoretically (e.g., Refs. 27–34). The easy-plane magnetization curves are close in shape to the Langevin curve describing magnetization of an ensemble of superparamagnetic particles:[35]

$$M = N\mu V L, \tag{2}$$

where

$$L = \coth\frac{\mu V H}{k_B T} - \frac{k_B T}{\mu V H}, \tag{3}$$

$N$ is the number of particle, $\mu$ and $V$ are the particle spontaneous magnetization and the mean volume, accordingly, $k_B$ is the Boltzmann constant, $T$ is temperature, and $H$ is the external magnetic field. A similar picture is observed for other samples.

The best fits of Eqs. (2) and (3) to the experimental dependencies $M(H)$ shown in Fig. 4 give the $\mu V$ values presented in Table I. Only for sample D1 synthesized with lower implantation dose, the $M(H)$ dependence is absolutely typical for superparamagnetic case (curve 1 in Fig. 4). For two other samples, the experimental curves (2 and 3 in Fig. 4) deviate from the classic Langevin curve. Such deviations were observed several times by other authors for different nanoparticle systems (see, e.g., Refs. 22,36, and 37). For instance, the magnetite fine particles behavior was analyzed in Ref. 37 using static magnetic measurements of particles both in the form of powder and dispersed in liquid and solid media. The magnetization curve deviations from the pure Langevin type were estimated with the help of the field dependence of the magnetic susceptibility $\chi(H)$ obtained from $M(H)$ curves

$$R = 1 - \frac{\int_0^{H_{\max}} \chi_{\text{expt}}(H)dH}{\int_0^{H_{\max}} \chi_{\text{Langevin}}(H)dH}, \tag{4}$$

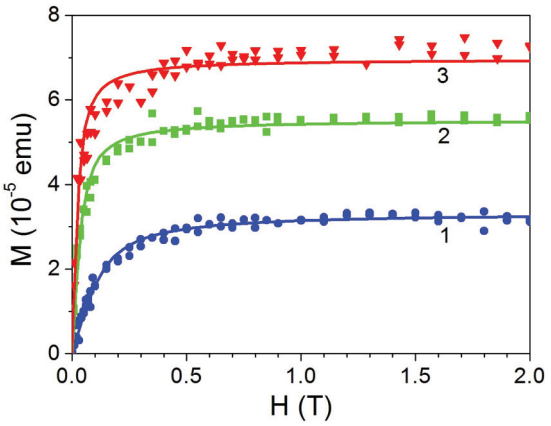


FIG. 4. (Color online) Room-temperature magnetization curves of samples D1–D3, curves 1–3, correspondingly. Solid lines are Eqs. (2) and (3), the best fits to the experimental curves.

where $\chi_{\text{expt}}(H)$ and $\chi_{\text{Langevin}}(H)$ are the experimental dependence and theoretical curve obtained by fitting the experimental points in the magnetic field values exceeding the field value corresponding to the susceptibility maximum. Following Ref. 37, we have evaluated the deviations in magnetic properties of the samples investigated from the pure Langevin type as $R = 0.0009$, 0.0099, and 0.0178 for samples D1–D3, correspondingly.

The magnetization temperature dependencies $M(T)$ recorded in a relatively low magnetic field for field-cooled (FC) and zero-field-cooled (ZFC) regimes of the sample cooling demonstrate the difference typical of superparamagnetic substances (Fig. 5). In ZFC curves, the peaks characteristic of superparamagnetic systems are observed at temperatures of 25, 40, and 70 K for samples D1, D2, and D3, respectively. The center of gravity of these peaks corresponds to the mean blocking temperatures $T_{b,\text{mean}}$ of each sample. The width of the peak reflects the distribution of blocking temperatures of each sample due to the distribution of particle size (see Fig. 3). For the simplest case of uniaxial single-domain nanoparticles,[35]

$$T_b = \frac{K_{\text{eff}} V}{25 k_B}, \tag{5}$$

where $K_{\text{eff}}$ is the effective anisotropy constant. The $K_{\text{eff}}$ values estimated according to Eq. (5), with $T_b$ determined as the temperature of the ZFC curves' maximum position (Fig. 5), are presented in Table I. These values exceed approximately by two orders of magnitude the bulk Ni anisotropy second constant.[24] The effective anisotropy is especially high for sample D1 with the smallest nanoparticles. The observations correlate with data of several authors who showed that magnetic anisotropy of small particles was larger than that of the bulk samples because of the symmetry loss at the particle surface (e.g., Refs. 38 and 39). Note that the shape of the $M(T)$ curve at temperatures exceeding $T_b$ corresponds to the pure superparamagnetic case for sample D1 only. For samples D2 and D3, this shape deviates from the superparamagnetic type just like the $M(H)$ curves (Fig. 4, curves 2 and 3).

At temperatures lower than $T_b$, hysteresis loops occur (Fig. 6) with the coercive field ($H_c$) increasing gradually when the temperature decreases. At $T = 5$ K, $H_c$ is about 0.025 T and the remanent magnetization $M_r$ equaled approximately 0.5 of the saturation magnetization value $M_s$ (Fig. 5). So, at low temperatures, nanoparticles in each sample are in the frozen state, and the $H_c$ and $M_r$ values are determined by the distribution of their in-plane anisotropy easy axes. The

TABLE I. Characteristics of Ni nanoparticles' ensembles.

| | D1 | D2 | D3 |
|---|---|---|---|
| Particles mean diameter ($10^{-7}$ cm) | ~3 | 6.7 | 7.8 |
| Particles mean volume ($10^{-19}$ cm$^3$) | | 5.61 | 9.47 |
| Maximal core diameter ($10^{-7}$ cm) | | 4 | 6 |
| Core-shell particles mean diameter ($10^{-7}$ cm) | | 8.2 | 9.8 |
| $\mu\langle V\rangle$ ($10^{-17}$ G cm$^3$) | 0.59 | 2.85 | 7.77 |
| $T_B$ (K) | 25 | 40 | 70 |
| $K_{\text{eff}}$ ($10^5$ erg/cm$^3$) | | 2.46 | 2.55 |
| $R$ (deviation from Langevin behavior) | 0.0009 | 0.0099 | 0.0178 |

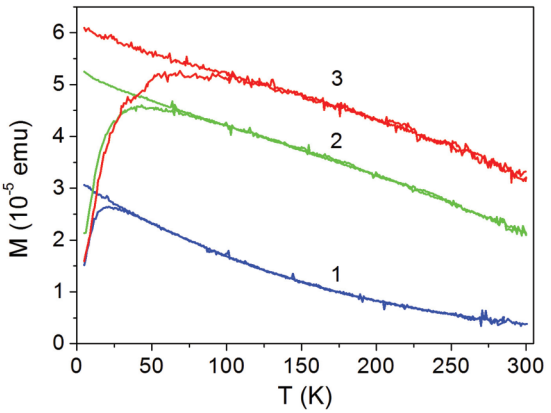


FIG. 5. (Color online) Experimental FC and ZFC magnetization temperature dependencies for samples D1–D3, curves 1–3, respectively, recorded in the magnetic field 0.02 T in the course of sample heating.

deviation of the experimental $M(H)$ and $M(T)$ curves from the classic superparamagnetic behavior becomes more evident with the implantation dose increase (Figs. 4 and 5).

Deviations of the fine-particle system magnetization behavior from the Langevin-type dependence were observed by many authors, and the interparticle interactions were considered more often to be responsible for such a deviation (e.g., Refs. 37,40–44, and references herein). Estimating qualitatively the influence of interparticle dipole-dipole interactions on the particle ensemble magnetic behavior, the authors of Ref. 37 proceeded from the energy $E$ of a particle within the system:

$$E = \frac{K_{\text{eff}} V}{2} + \frac{\mu_0}{2\pi}\frac{m^2}{d^3} + \mu_0 m H, \tag{6}$$

where the first term is the magnetic crystalline anisotropy energy ($E_K$) of a particle material, the second term is the dipole-dipole interaction energy ($E_{d\text{-}d}$) between the particles, and the third term is the energy of interaction between the magnetic dipole and the external magnetic field ($E_H$), $d$ is the mean distance between the magnetic moments corresponding to each particle, $\mu_0$ is the absolute permeability of vacuum, and $m = \mu V$. To rotate the magnetic moment of a particle to the external magnetic field direction, the mean magnetic energy should be larger (or, at least equal) compared to the sum of $E_K$ and $E_{d\text{-}d}$:

$$E_H \geqslant E_K + E_{d\text{-}d}. \tag{7}$$

Under this condition, the nanoparticle behavior in the magnetic field will follow the Langevin law.

As to our samples, we shall estimate the role of dipole-dipole interaction using calculated $K_{\text{eff}}$ and $\mu = 58.57 \pm 0.03$ emu/g (Ref. 45) for Ni and taking nanoparticle characteristics $V$ and $d$ from the electron microscopy images. A simple calculation according to Eq. (5) gives $E_K = 6.9 \times 10^{-14}$ erg and $E_{d\text{-}d} = 1 \times 10^{-15}$ erg for the sample D2 and $E_K = 1.2 \times 10^{-13}$ erg and $E_{d\text{-}d} = 3 \times 10^{-15}$ erg for the sample D3, that is, the interparticle interaction energy is essentially lower comparing to the crystalline anisotropy energy. So, the interparticle interaction can hardly be considered as the main mechanism affecting in the deviation of the magnetization temperature dependence from the Langevin behavior.

It is generally accepted that, at the surface of the particles, the broken translation symmetry and the lower coordination of magnetic atoms strongly affect the particle magnetic behavior (e.g., Ref. 46). In particular, anisotropy energy per atom at the surface can be two or three orders of magnitude larger than that in a bulk crystal, causing an anisotropy enhancement in the whole nanoparticle.[38,39,47,48] The role of surface should increase for the core-shell nanoparticles because of the larger proportion of the lower coordinated spins located at the inner and the outside surfaces of the shell. Studying the core-shell maghemite nanoparticles, the authors of Ref. 49 made an estimation of the anisotropy energy per unit volume which appeared to be one order of magnitude larger than that of solid nanoparticles, and two orders of magnitude larger than that of the bulk maghemite. As it was shown above, the Ni nanoparticles' anisotropy determined with the help of the ZFC magnetization temperature dependence (Fig. 5) and the average particles' volume (Table I) exceeded approximately by two orders of magnitude the bulk Ni single-crystal anisotropy. The finding correlates well with the results of Ref. 49. Note that the core-shell nanoparticles in our samples coexist with the solid nanoparticles. It will lead to the dispersion of the particle anisotropy values affecting the magnetization temperature dependence deviation from that for the pure superparamagnetic case.

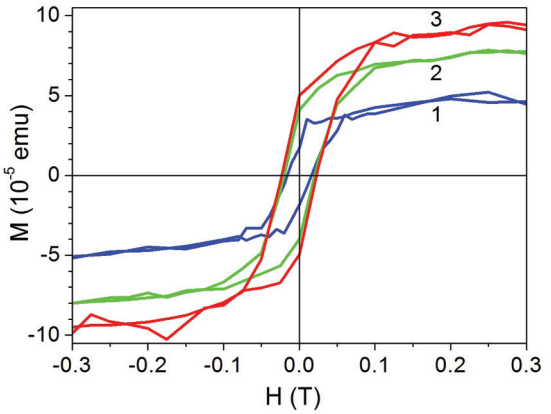


FIG. 6. (Color online) Hysteresis loops 1–3 for samples D1–D3, correspondingly, measured at $T = 5$ K in the plane geometry.

## V. MAGNETO-OPTICS

FR spectra of the samples investigated (Fig. 7) demonstrate strong, broad maximum centered near 3 eV and shifting slightly to lower energies with the implantation dose increase. In the spectral interval 1.7–2.0 eV, FR changes sign. The point where FR passes through zero also shifts to lower energies with the implantation dose increase. MCD spectral dependencies for the D1–D3 samples are presented in Fig. 8. Two distinct extremes are seen in the MCD spectra: one negative centered near 2.0 eV and the second positive centered in the vicinity of 3.5 eV. MCD changes sign in three energy intervals: near 1.25, at ~3.1–3.4, and near 4.0 eV. At that, the middle zero-crossing point (~3.1–3.4 nm) as well the negative and positive MCD maximum positions shift to lower energies with the implantation dose increase similar to the characteristic

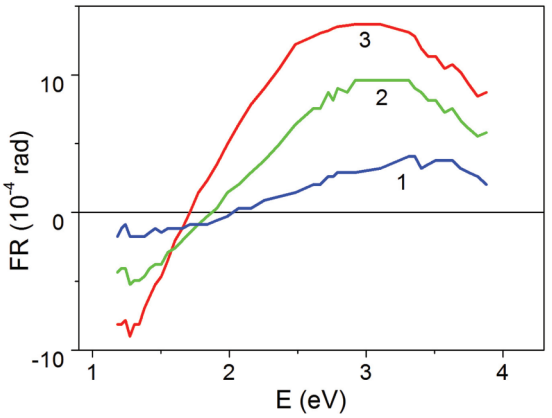


FIG. 7. (Color online) Room-temperature FR spectral dependencies of samples D1–D3, curves 1–3, respectively, in the magnetic field 0.3 T.

points in the FR spectra. The middle MCD zero-crossing point (∼3.1–3.4 nm) corresponds to the maximum position in the FR spectra in accordance with Kramers-Kronig relations (e.g., Ref. 50, "section 7.10").

The implanted samples FR spectra differ essentially from that of the continuous Ni film, presented in the classic work (Ref. 51): FR of Ni films measured in the magnetic field directed normally to the film plane was characterized by maximum near 1.2 eV followed by the gradual reduction at the light wavelength decrease. We failed in searching MCD data for the Ni films in literature and made measurements in specially prepared Ni film of 20 nm in thickness. The MCD spectrum obtained for this film (Fig. 9) seems to consist of two broad overlapping bands centered at approximately 1.7 and 3.2 eV. Near energy 1.3 eV, MCD changes sign. The Ni film MCD spectrum resembles in shape the polar Kerr effect (PKE) spectrum of the polished bulk Ni samples[52–54] and thin Ni films presented in Refs. 18,51,55–59 with two maxima (of negative sign) at approximately 1.5 and 3.2 eV and the sign changes near 1 and 4 eV. Note that the PKE spectra obtained by different authors both for the bulk Ni and thin Ni films, including our film, correlate with each other very well.

The coincidence of the Ni film MCD spectrum (Fig. 8) and the PKE spectra presented in the above-mentioned references

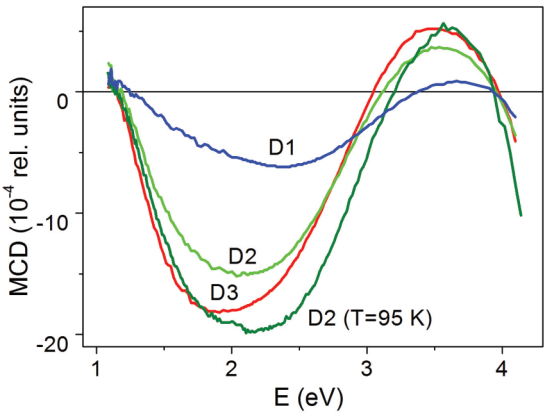


FIG. 8. (Color online) MCD spectra for samples D1–D3 at $T = 300$ K, and for D2 at $T = 95$ K. $H = 0.3$ T.

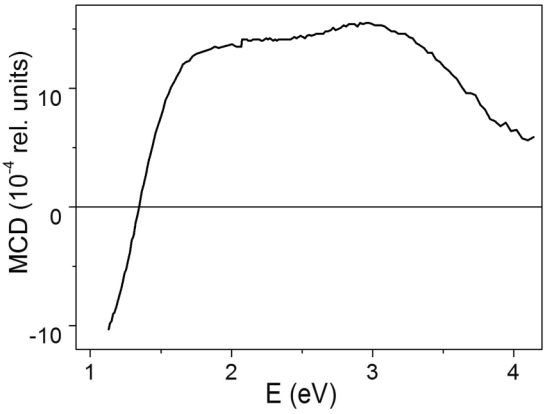


FIG. 9. Room-temperature MCD spectrum of the continuous Ni film of 20 nm thick, $H = 0.3$ T.

is not surprising: both effects are mainly due to the imaginary part of the nondiagonal component $\varepsilon''_{xy}$ of the dielectric tensor $\hat{\varepsilon}$ that can be written for the case of a sample with spherical or cubic symmetry and magnetic field directed along the $z$ axis as

$$\hat{\varepsilon} = \begin{bmatrix} \varepsilon_{xx} & i\varepsilon_{xy} & 0 \\ -i\varepsilon_{yx} & \varepsilon_{yy} & 0 \\ 0 & 0 & \varepsilon_{zz} \end{bmatrix}. \quad (8)$$

At that, the components $\varepsilon_{xx} = \varepsilon_{yy}$; $\varepsilon_{zz}$ can differ from two first-diagonal components when the substance possesses magnetic linear birefringence and dichroism. The real ($\varepsilon'_{xx}$) and imaginary ($\varepsilon''_{xx}$) parts of the diagonal components are associated with the complex refractive index $\eta = n - ik$ by the expressions $\varepsilon'_{xx} = n^2 - k^2$, $\varepsilon''_{xx} = 2nk$. The imaginary part of the nondiagonal component $\varepsilon''_{xy}$ is responsible for the difference in the absorption of right- and left-circularly polarized light.

The origin of the features in the PKE spectra of the continuous Ni films and polished bulk samples are questionable up to now. The shape of the PKE and $\varepsilon''_{xy}$ spectra calculated by different authors (see Refs. 60 and 61 and references within) correlates fairly well with the experimental ones in the interval ∼0.5–3.5 eV. But, the maxima in the calculated spectra have larger amplitudes than the experimental ones, and the peak positions are shifted toward higher energies. At higher energies, the disagreement between the calculated and experimental PKE spectra becomes more pronounced (Fig. 5 in Ref. 61). As far as the origin of the maxima is concerned, they were attributed, in general, to interband and intraband electron transitions. For instance, in Ref. 51, they were attributed to the electron transitions between the minority- and majority-spin bands at different symmetry points: the minority-spin transitions were supposed to produce the first negative (0.5 eV) and the second (3.2 eV) positive peaks in the PKE spectrum, and the majority-spin transitions the first positive (1.5 eV) and the second negative (4.5 eV) peaks.

When changing the course of the discussion from the bulk metal to this metal nanometric particle, one will think on the possibility of the surface plasmon resonance (SPR) excitation. SPR excitation, first put forward by Mie,[62] is one of the mechanisms considered by many authors to be responsible

for the peculiarities in the optical spectra of small metal, mainly noble, particles (e.g., Refs. 63 and 64). Several authors observed peculiarities being due to SPR excitation in the optical absorption spectra of the Ni nanoparticle ensembles in different matrices. The absorption spectra of Ni nanoparticles synthesized in the $SiO_2$ matrix under the conditions most similar to our case were presented in Refs. 65 and 66. Two prominent maxima were observed in the spectrum at the light wave energies of 3.6 and 5.8 eV in Ref. 65. In Ref. 66, a shoulder at ∼3 eV and peak at ∼6 eV were observed. The lower-energy peak (3.6 or 3.3. eV) was attributed to the SPR absorption in both papers, while the second one was explained as having originated from the interband transition $L_2' \rightarrow L_1$ in Ref. 65 and as being of the unknown nature in Ref. 66. Similar peculiarities in the absorption spectra of Ni nanoparticles grown in silica glass by annealing sol-gel prepared silicate matrices doped with nickel nitrate were obtained in Ref. 67: at energy 3.47 eV, which was associated with SPR excitation, and at 6 eV, which was considered as light absorption by NiO clusters dispersed in the silica matrix in accordance with the results of Refs. 68–70. Besides, two more features were seen in the absorption spectra at 1.97 and 2.35 eV. They were attributed to the light absorption by $Ni^{2+}$ ions in tetrahedral coordination according to Refs. 68 and 71. In Ref. 67, it was also shown that the width of the SPR absorption band decreases with the temperature decrease and with the particle-size increase. Note that the nanoparticle ensembles prepared by the sol-gel technique are characterized by significantly narrower particle-size distribution compared to that in the ensembles fabricated with the ion implantation. This circumstance can explain why some of the absorption peaks are not observed in the ion-implanted samples[65,66] and others are broader compared to the samples prepared by the sol-gel method.

Since the magneto-optical technique is more sensitive compared to optical absorption, one can expect that MCD and PKE maxima can be distinctly observed in the spectral regions where the absorption peaks are smoothed because of their overlapping. At least two papers are available in literature dealing with magneto-optical spectra of Ni nanoparticles embedded in dielectric matrix.[18,72] The PKE spectrum of nickel nanoparticles (2.9 nm of mean diameter) in silica glasses ($SiO_2$) fabricated by the implantation of Ni negative ions of 60 keV is presented in Ref. 18 and MCD spectra of colloidal liquid dispersions of Ni nanoparticles with the size equal or below 15 nm synthesized by a ligand stabilized solution-phase synthesis are considered in Ref. 72. Due to the high opaqueness of the samples in the higher-energy interval of the spectrum, MCD was recorded[72] in a narrower spectral interval (∼1.5–3.2 eV) compared to the PKE spectrum.[18] In this interval, MCD and PKE spectra coincide totally with each other like the continuous Ni films considered above and differ essentially from the spectra of a continuous Ni film (compare Figs. 3 and 4 in Ref. 18). The spectra presented in this interval by a broad nonsymmetrical maximum cover the whole interval. The maximum position, 3.2 eV, is very close to the SPR peak position observed for Ni nanoparticles by several authors (e.g., Refs. 65,66,73, and 74). Additional peaks are seen in the Ni nanoparticles' PKE spectrum at ∼4 eV (negative) and 5.4 eV (positive).[18] The nature of the MCD maximum at 3.2 eV is not discussed in Ref. 72. The PKE spectrum is considered in Ref. 18 as a sum of size-sensitive free-electron contribution and size-insensitive bound-electron contribution. The authors of Ref. 18 calculated PKE spectra of Ni nanoparticles depending on the particle dimension using the Lissberger and Saunders approach[75] for the free-electron contribution with the inclusion of the bound-electron contribution. They obtained, in particular, the moderate red-shift of the spectrum with the particle-size decrease (Fig. 5 in Ref. 18).

Discussing MCD spectra of the Ni-implanted samples investigated, one can note their difference from both MCD and PKE spectra of the continuous Ni films and the solid Ni nanoparticles. It seems to be reasonable to attribute the difference to the core-shell nanoparticles' morphology.

Generally, MCD spectral dependence of the electron transition from $a$ to $j$ state (further, we shall omit indices $a \rightarrow j$ at the corresponding values such as $\omega_{a\rightarrow j}$, and so on) is described by the expression[76]

$$\theta = -\frac{4\pi}{\hbar c} N \left[ A \frac{4\omega_0 \omega^3 \left(\omega_0^2 - \omega^2\right)\gamma}{\hbar\left[\left(\omega_0^2 - \omega^2\right)^2 + \omega^2\gamma^2\right]^2} + \left(B + \frac{C}{kT}\right) \frac{\omega^3 \gamma}{\left(\omega_0^2 - \omega^2\right)^2 + \omega^2\gamma^2} \right] M_z(H), \qquad (9)$$

where $\hbar$ is the Planck's constant, $c$ is the light speed, $N$ is a number of the active centers, $A$, $B$, $C$ are the parameters determined by the electron transition matrix elements, $M_z$ is the magnetization component (depending on the magnetic field $H$) along the direction of the light wave propagation, $k$ is Boltzmann constant, $T$ is temperature, $\omega_0$ is the frequency of the transition from the ground to the excited state, $\omega$ is the current frequency, and $\gamma$ is the linewidth of the transition. The term $A$ arises from transitions involving degenerate excited states, its shape corresponds to a first derivative of an absorption line, i.e., MCD equals zero at the energy of the absorption maximum. The term $B$ arises from magnetically induced mixing of no degenerate states, and the shape is similar to that of the absorption band. Both $A$ and $B$ terms do not depend on temperature. The term $C$ arises from transitions involving degenerate ground states; this term depends on temperature and is determined by the difference of the population of the ground-state splitting components. $A$, $B$, and $C$ are called diamagnetic, mixing, and paramagnetic terms, correspondingly.

Comparing temperature dependencies of different terms in (9) with the intensities of the MCD maxima observed in the samples investigated (Fig. 8), we can consider MCD to be of the paramagnetic character. The shape of the paramagnetic MCD spectrum depends on the ratio between the optical absorption band width ($\gamma$) and its splitting ($\omega_{0+} - \omega_{0-}$) under the action of a magnetic field or spontaneous magnetization. In the case $(\omega_{0+} - \omega_{0-}) \ll \gamma$, the bell-shaped MCD maxima should be observed at wavelength energies very close to the absorption maxima energies. One of the possible scenarios explaining the observed MCD spectra is based on the association of positive and negative MCD maxima with the different absorption bands. To realize it, we made the deconvolution of experimental MCD spectra to separate Gaussian components.

TABLE II. Parameters of Gaussians best fitted to the experimental curves.

| | | G1 | | | G2 | | | G3 | | | G4 | |
|---|---|---|---|---|---|---|---|---|---|---|---|---|
| Sample | $E$ (eV) | $I \times 10^{-4}$ | $\Gamma$ (eV) | $E$ (eV) | $I \times 10^{-4}$ | $\Gamma$ (eV) | $E$ (eV) | $I \times 10^{-4}$ | $\Gamma$ (eV) | $E$ (eV) | $I \times 10^{-3}$ | $\Gamma$ (eV) |
| D1 ($T = 300$ K) | 1.1 | 1 | 0.48 | 2.73 | −18 | 1.72 | 3.48 | 10 | 1.24 | 6 | −10 | 1.66 |
| D2 ($T = 300$ K) | 1.06 | 6 | 0.51 | 2.45 | −45 | 2.02 | 3.34 | 23 | 1.18 | 6 | −15 | 1.64 |
| D2 ($T = 90$ K) | 1.1 | 7 | 0.49 | 2.5 | −63 | 2.28 | 3.61 | 44 | 1.23 | 6 | −20 | 2.41 |
| D3 ($T = 300$) K | 1.09 | 7 | 0.45 | 2.19 | −54 | 2.21 | 3.34 | 24 | 1.15 | 6 | −20 | 1.57 |

The best fit of the experimental curves to the calculated sums of four Gaussians (G1–G4) was obtained with the Gaussian parameters collected in Table II. Peaks G1 and G4 are situated beyond the spectral interval of investigation, but their insertion was necessary to describe the experimental spectrum adequately. An example of the fitting is shown in Fig. 10 for sample D2. To fit MCD curves, the energy of peak G4 was fixed as 6.0 eV according to Refs. 65–67 and its intensity was limited by the value exceeding that of the G2 peak intensity not more than three to five times. All parameters of peaks G1−G3 and the width of peak G4 were varied. Note that the sum of the G2 and G3 peak modules will be centered near the energy 3 eV. This energy value is close to the peculiarity energy observed in the absorption spectra in Refs. 65–67, which was ascribed to SPR excitation.

The analyses of the G2–G3 peak parameters obtained show the increase of intensity with the dose increase and with the temperature decrease. The last circumstance approves the paramagnetic character of these peaks. The peak width increases for G2 and decreases for G3 with the implantation dose increase. Peak G2 shifts significantly to the lower energies with the implantation dose increase (2.73, 2.45, 2.19, correspondingly). Peak G3 shifts only slightly when coming from the D1 to D2 sample, and does not change at the further dose increase; its position coincides with the SPR position presented in Ref. 67. Thus, this peak originated, more probably, from the SPR excitation in solid nanoparticles. Not only its position but also its narrowing with the temperature decrease favors such a relation. The fact that MCD changes sign at ∼4 eV evidences the existence of the MCD negative maximum (and, consequently, the absorption maximum) at higher energies. Indeed, the narrow negative peak was observed in the PKE spectrum of Ni implanted in $SiO_2$ nanoparticles.[18] Note this peak position to be very close to an analogous peak position in thin Ni film[18] and bulk crystals.[50,52] It can be associated with a strong absorption band near 6 eV observed in Refs. 65 and 66 and attributed there to the bound electron absorption. Finally, the broader negative maximum at ∼2.5 eV can reasonably be attributed to SPR in the core-shell Ni nanoparticles. The surface-mediated surface-plasmon resonance conditions were presented in Ref. 77 for composites of nanospheres which consisted of a core and shell, in particular, a metallic shell and dielectric core suspended in a dielectric medium. General expressions were given in Ref. 78 for the local-field enhancement, absorption, and nonlinear optical response in metal-coated nanoparticles depending on the particle core-shell ratios. The absorption spectra of nanoparticles consisting of metal shell and nonmetal core were investigated experimentally and theoretically for gold-coated nanoparticles.[79] The authors observed two bands in the absorption spectrum of the samples containing pure gold nanoparticles and gold-coated $Au_2S$ nanoparticles. The relatively narrow band at higher energy independent of the particles' size was associated with SPR in the pure gold particles, while the lower-energy broader peak shifted along the energy axis depending on the core-shell ratio was attributed to SPR in the coated particles. MCD spectra in our samples correspond qualitatively to the results of the cited papers: the SPR bands associated with the metal-coated nanoparticles are centered at lower energies comparing to the SPR band in the solid (pure metal) nanoparticles; its energy position depends on the core-shell radii ratio and shifts to higher energy as this ratio decreases.

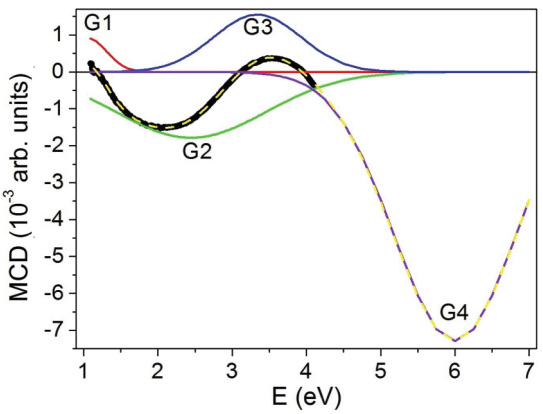


FIG. 10. (Color online) The deconvolution components G1–G4, summation curve (dashed line), and the experimental curve (black bold line) for sample D2 at $T = 300$ K.

Using the approach of Ref. 77, we estimated the dispersion of the electric-field magnitude associated with the core-shell nanoparticles in our samples according to the formula

$$E_1 = \frac{9\varepsilon_2\varepsilon_3}{\varepsilon_2\varepsilon_a + \varepsilon_3\varepsilon_b} E_0(\cos\theta\hat{e}_r - \sin\theta\hat{e}_0), \tag{10}$$

where $r_1$ and $r_2$ are the spherical core and shell radii, correspondingly, $\varepsilon_1$, $\varepsilon_2$, $\varepsilon_3$ are dielectric permittivities of the inner sphere, the shell, and the outer suspending medium, $\theta$ is the angle between the generated field direction and the incident-field polarization direction,

$$\begin{aligned} \varepsilon_a &= \varepsilon_1(3-2P) + 2\varepsilon_2 P, \\ \varepsilon_b &= \varepsilon_1 P + \varepsilon_2(3-P), \\ P &= 1-(r_1/r_2)^3. \end{aligned} \tag{11}$$

$E_0$ is the field far from the particle.

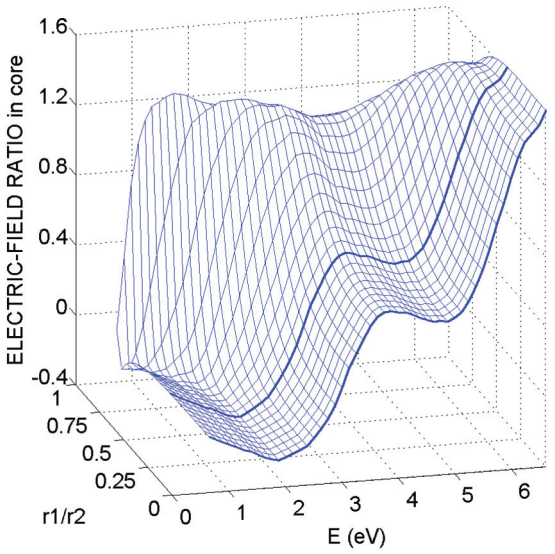


FIG. 11. (Color online) Magnitude of the electric-field ratio $E_1/E_0$ in the core region depending on the light energy with the $r_1/r_2$ ratio as a parameter. The curves for $r_1/r_2 = 0.4$ and $r_1/r_2$ close to zero are marked out with bold.

The inner sphere was supposed to consist of $SiO_2$ just as the outer suspending medium with the dielectric permittivity of 2.25, the Ni shell optical constants were taken from Ref. 80. Values were taken from the TEM images' analysis.

The obtained resonant behavior of the electric-field ratio $E_1/E_0$ in the core region as a function of the electromagnetic wave energy with the ratio $r_1/r_2$ as a parameter is shown in Fig. 11. Note the value $r_1/r_2 = 1$ corresponds to the spherical pure dielectric particle (without the metal shell), and the value $r_1/r_2 = 0$ corresponds to the spherical metal particle (without the dielectric core). It is seen that for the core-shell particles with the $r_1/r_2$ ratio close to ~0.4, characteristic for samples D2 and D3, the electric-field resonance is expected to take place at about 2.5 eV. The narrower peak at about 3.5 eV corresponds to $r_1/r_2$ close to zero, i.e., to the pure metal nanoparticles. Just the same picture is observed in the experiment. So, the MCD maxima can be associated with the SPR excitations in the pure Ni and core-shell nanoparticles.

## VI. CONCLUSION

In summary, we have presented morphology, magnetic, and magneto-optical properties of the ensembles of Ni nanoparticles fabricated with fast $Ni^+$-ion implantation into an amorphous fused silica ($SiO_2$) substrate. The implantation doses were $0.5 \times 10^{17}$, $0.75 \times 10^{17}$, and $1 \times 10^{17}$ $Ni^+/cm^2$. Using TEM of the cross section of a sample, we showed that the implantation resulted in the formation of spherical metallic nickel nanoparticles in the implanted surface layer. The nanoparticles have the fcc structure with the lattice parameters close to the bulk Ni, and their sizes vary from 2 to 16 nm depending on the implantation dose (amount of introduced magnetic nickel). The larger particles were shown to have core-shell morphology with the core containing no Ni and consisting supposedly of $SiO_2$, while Ni is gathered in the shell. Generally speaking, the formation of core-shell nanoparticles is not characteristic of the implantation conditions used. The origin of such a phenomenon is discussed. The core-shell nanoparticles essentially affect the magnetic and magneto-optic properties of the composite samples. The magnetic measurements showed that the nanoparticles are in the superparamagnetic state at room temperature and passed into "the frozen" state at different temperatures depending on the implantation dose. But, the shape of the ZFC curve coincides with that for pure superparamagnetic medium only for the sample implanted with the lowest dose. To explain the ZFC curve deviation from the classic superparamagnetic type, we evaluated the possible contribution of the interparticle interaction and showed this deviation to be due to the core-shell particle structure rather than interparticle interaction.

In the spectral range 1.1–4.2 eV, we studied the effect of the implantation dose on the MCD in a composite $SiO_2$ layer containing implanted nickel nanoparticles. The shape of the MCD spectra in the composite layer was found to be strongly modified as compared to those of a specially prepared continuous nickel film. MCD spectra of the implanted samples consisting of two wide maxima of the opposite sign were fitted by several Gaussians. The analysis of the Gaussian parameters' dependence on the implantation dose and temperature allowed associating the lower-energy MCD maximum with SPR excitation in the core-shell nanoparticles and the higher-energy maximum with SPR excitation in the pure Ni nanoparticles.

## ACKNOWLEDGMENTS

This work was supported by the Russian Foundation for Basic Research (Projects No. 11-02-00972, No. 12-02-31026, No. 12-02-97029, and No. 12-02-900528) and by the Russian President Grant No. NSh-1044.2012.2. A.L.S. is grateful to the Alexander von Humboldt Foundation, DAAD and DFG in Germany, Austrian Scientific Foundation in the frame of Lisa Meitner Fellowship, and the Royal Society in the UK for the financial support. S.M.Z. is grateful to the Ministry of Education and Science of the Russian Federation (FTP "Scientific and scientific-pedagogical personnel of the innovative Russia, 2009-2013") and Presidium RAS Project No. 24.34 for the financial support.

[1] O. A. Aktsipetrov, E. M. Kim, R. V. Kapra, T. V. Murzina, A. F. Kravets, M. Inoue, S. V. Kuznetsova, M. V. Ivanchenko, and V. G. Lifshits, Phys. Rev. B **73**, 140404(R) (2006).

[2] D. J. Sprouster, R. Giulian, L. L. Araujo, P. Kluth, B. Johannessen, D. J. Cookson, G. J. Foran, and M. C. Ridgway, J. Appl. Phys. **107**, 014313 (2010).

[3] S. Zhu, X. Xiang, X. T. Zu, and L. M. Wang, Nucl. Instrum. Methods Phys. Res., Sect. B **242**, 114 (2006).

[4] T. Lutz, R. Poinsot, J. L. Guille, and C. Estournes, J. Non-Cryst. Solids **351**, 3023 (2005).

[5] P. Chakraborty, J. Mater. Sci. **33**, 2235 (1998).

[6] D. Kechrakos and K. N. Trohidou, Phys. Rev. B **71**, 054416 (2005).

[7] J. C. Denardin, M. Knobel, X. X. Zhang, and A. B. Pakhomov, J. Magn. Magn. Mater. **262**, 15 (2003).

[8] J. Z. Zhang, *Optical Properties and Spectroscopy of Nanomaterials* (World Scientific, Singapore, 2009).

[9] P. T. Townsend, P. J. Chandler, and L. Zhang, *Optical Effects of Ion Implantation* (Cambridge University Press, Cambridge, UK, 1994).

[10] J. Davenas, A. Perez, P. Thevenard, and C. H. S. Dupuy, Phys. Status Solidi A **19**, 679 (1973).

[11] E. Cattaruzza, Appl. Phys. Lett. **73**, 1176 (1998).

[12] A. Meldrum, R. F. Haglund Jr., L. A. Boatner, and C. W. White, Adv. Mater. **13**, 1431 (2001).

[13] F. Gonella, Rev. Adv. Mater. Sci. **14**, 134 (2007).

[14] I. S. Edelman, D. A. Petrov, R. D. Ivantsov, S. M. Zharkov, R. I. Khaibullin, V. F. Valeev, V. I. Nuzhdin, and A. L. Stepanov, J. Exp. Theor. Phys. **113**, 1040 (2011).

[15] A. L. Stepanov, *Ion-Synthesis of Silver Nanoparticles and Their Optical Properties* (Nova Science, New York, 2010).

[16] A. L. Stepanov, D. E. Hole, and P. D. Townsend, Nucl. Instrum. Methods Phys. Res., Sect. B **149**, 89 (1999).

[17] U. Kreibig and M. Vollmer, *Optical Properties of Metal Clusters* (Springer, Berlin, 1995).

[18] H. Amekura, Y. Takeda, and N. Kishimoto, Thin Solid Films, **464-465**, 268 (2004).

[19] H. Amekura, Y. Takeda, K. Kono, and N. Kishimoto, Trans. Mater. Res. Soc. Jpn. **29**, 615 (2004).

[20] C. Görller-Walrand and K. Binnemans, *Magnetic Circular Dichroism in Transparent Rare-Earth Compounds*, Encyclopedia of Materials: Science and Technology, 9414 (Elsevier, Amsterdam, 2001).

[21] A. L. Stepanov, Rev. Adv. Mater. Sci. **26**, 1 (2010).

[22] C. Fernandez, M. A. Tagliente, G. Mattei, C. Sada, V. Bello, C. Maurizio, G. Battaglin, C. Sangregorio, D. Gatteschi, L. Tapfer, and P. Mazzoldi, Nucl. Instrum. Methods Phys. Res., Sect. B **216**, 245 (2004).

[23] T. S. Anderson, R. H. Magruder, D. L. Kinser, J. E. Wittig, R. A. Zuhr, and D. K. Thomas, J. Non-Cryst. Solids **224**, 299 (1998).

[24] G. Mattei, G. Battaglin, V. Bello, E. Cattaruza, C. De Julian, G. De Marchi, C. Maurizio, P. Mazzoldi, M. Parolin, and C. Sada, Nucl. Instrum. Methods Phys. Res., Sect. B **218**, 443 (2004).

[25] F. Ren, X. H. Xiao, G. X. Cai, J. Wang, and C. Z. Jiang, Appl. Phys. A **96**, 317 (2009).

[26] F. Ren, C. Jiang, C. Liu, and J. Wang, Phys. Rev. Lett. **97**, 165501 (2006).

[27] I. S. Edelman, E. A. Petrakovskaja, D. A. Petrov, S. M. Zharkov, R. I. Khaibullin, V. I. Nuzhdin, and A. L. Stepanov, Appl. Magn. Reson. **40**, 363 (2011).

[28] U. Netzelmann, J. Appl. Phys. **68**, 1800 (1990).

[29] M. Rubinstein, B. N. Das, N. C. Koon, D. B. Chrisey, and J. Horwitz, Phys. Rev. B **50**, 184 (1994).

[30] Y. W. Yu, J. W. Harrell, and W. D. Doyle, J. Appl. Phys. **75**, 5550 (1994).

[31] J. Dubowik, Phys. Rev. B **54**, 1088 (1996); **62**, 727(E) (2000).

[32] R. I. Khaibullin, L. R. Tagirov, B. Z. Rameev, Sh. Z. Ibragimov, F. Yildiz, and B. Aktas, J. Phys.: Condens. Matter **16**, L443 (2004).

[33] B. Rameev, C. Okay, F. Yildiz, R. I. Khaibullin, V. N. Popok, and B. Aktas, J. Magn. Magn. Mater. **278**, 164 (2004).

[34] C. Okay, B. Z. Rameev, R. I. Khaibullin, M. Okutan, F. Yildiz, V. N. Popok, and B. Aktas, Phys. Status Solidi A **203**, 1525 (2006).

[35] C. P. Bean, J. Appl. Phys. **26**, 1381 (1955).

[36] X. Batlle and A. Labarta, J. Phys. D: Appl. Phys. **35**, R15 (2002).

[37] I. Malaescu and C. N. Marin, J. Magn. Magn. Mater. **218**, 91 (2000).

[38] E. L. Duarte, R. Itri, E. Lima, Jr., M. S. Baptista, T. S. Berquo, and G. F. Goya, Nanotechnology **17**, 5549 (2006).

[39] R. Yanes, O. Chubykalo-Fesenko, H. Kachkachi, D. A. Garanin, R. Evans, and R. W. Chantrell, Phys. Rev. B **76**, 064416 (2007).

[40] J. L. Dorman, A. Ezzir, R. Cherkaoui, M. Nogues, F. Lucari, F. d'Orazio, M. Godinho, E. Tronc, J. P. Jolivet, and D. Fiorani, J. Phys. IV **7**, 509 (1997).

[41] K. O'Grady, M. El-Hilo, and R. W. Chantrell, IEEE Trans. Magn. **29**, 2608 (1993).

[42] J. L. Dormann, F. D'Orazio, F. Lucari, E. Tronc, P. Prene, J. P. Jolivet, D. Fiorani, R. Cherkaoui, and M. Nogues, Phys. Rev. B **53**, 14291 (1996).

[43] M. F. Hansen and S. Morup, J. Magn. Magn. Mater **184**, 262 (1998).

[44] H. Kesserwan, G. Manfredi, J.-Y. Bigot, and P.-A. Hervieux, Phys. Rev. B **84**, 172407 (2011).

[45] R. M. Bozorth, J. Appl. Phys. **8**, 575 (1937).

[46] R. H. Kodama and A. E. Berkowitz, Phys. Rev. B **59**, 6321 (1999).

[47] M. Jamet, W. Wernsdorfer, C. Thirion, D. Mailly, V. Dupuis, P. Mélinon, and A. Pérez, Phys. Rev. Lett. **86**, 4676 (2001).

[48] P. Gambardella, S. Rusponi, M. Veronese, S. S. Dhesi, C. Grazioli, A. Dallmeyer, I. Cabria, R. Zeller, P. H. Dederichs, K. Kern, C. Carbone, and H. Brune, Science **300**, 1130 (2003).

[49] A. Cabot, A. P. Alivisatos, V. F. Puntes, L. Balcells, O. Iglesias, and A. Labarta, Phys. Rev. B **79**, 094419 (2009).

[50] J. D. Jackson, *Classical Electrodynamics*, 2nd ed. (Wiley, New York, 1975).

[51] K. H. Clemens and J. Jaumann, Z. Phys. **173**, 135 (1963).

[52] G. S. Krinchik and V. A. Artem'ev, JETP **53**, 1901 (1967) [Sov. Phys.–JETP **26**, 1080 (1968)].

[53] S. Krinchik and V. A. Artemjev, J. Appl. Phys. **39**, 1276 (1969).

[54] G. Q. Di and S. Uchiyama, J. Appl. Phys. **75**, 4270 (1994).

[55] J. L. Erskine and E. A. Stern, Phys. Rev. Lett. **30**, 1329 (1973).

[56] P. G. van Engen, K. H. J. Buschow, and M. Erman, J. Magn. Magn. Mater. **30**, 374 (1983).

[57] K. H. J. Buschow, *Ferromagnetic Materials*, edited by E. P. Wohlfarth and K. H. J. Buschow, Vol. 4 (North-Holland, Amsterdam, 1988).

[58] S. Visnovsky, V. Parizek, M. Nyvlt, P. Kielar, V. Prosser, and R. Krishnan, J. Magn. Magn. Mater. **127**, 135 (1993).

[59] K. Nakajima, H. Sawada, T. Katayama, and T. Miyazaki, Phys. Rev. B **54**, 15950 (1996).

[60] D. Sangalli, A. Marini, and A. Debernardi, Phys. Rev. B **86**, 125139 (2012).

[61] A. Delin, O. Eriksson, B. Johansson, S. Auluck, and J. M. Wills, Phys. Rev. B **60**, 14105 (1999).

[62] G. Mie, Ann. Phys. (NY) **25**, 377 (1908).

[63] H. Haberland, *Clusters of Atoms and Molecules II*, Vol. 56 of Springer Series in Chemical Physics (Springer, Berlin, 1994).

[64] G. Weick, Ph.D. thesis, Strasbourg, 2006, http://scd-theses.u-strasbg.fr/1153/01/thesis_Weick.pdf.

[65] T. Isobe, S. Y. Park, R. A. Weeks, A. Raymond, and A. Zuhr, J. Non-Cryst. Solids **189**, 173 (1995).

[66] H. Amekura, Y. Takeda, and N. Kishimoto, Nucl. Instrum. Methods Phys. Res., Sect. B **222**, 96 (2004).

[67] O. A. Yeshchenko, I. M. Dmitruk, A. A. Alexeenko, and A. M. Dmytruk, J. Phys. Chem. Solids **69**, 1615 (2008).

[68] C. R. Bamford, *Colour Generation and Control in Glass* (Elsevier, Amsterdam, 1977).

[69]R. J. Powell and E. Spicer, Phys. Rev. B **2**, 2182 (1970).
[70]R. Newman and R. M. Chrenko, Phys. Rev. **114**, 1507 (1959).
[71]J. Hernandez-Torres and A. Mendoza-Galvan, Thin Solid Films **472**, 130 (2005).
[72]O. Pascu, J. M. Caicedo, J. Fontcuberta, G. Herranz, and A. Roig, Langmuir **26**, 12548 (2010).
[73]C. F. Bohren and D. R. Huffman, *Absorption and Scattering of Light by Small Particles* (Wiley, New York, 1983).
[74]S. K. Sharma, P. Kumar, R. Kumar, M. Knobel, P. Thakur, K. H. Chae, W. K. Choi, R. Kumar, and D. Kanjilal, J. Phys.: Condens. Matter **20**, 285211 (2008).
[75]P. H. Lissberger and P. W. Saunders, Thin Solid Films **34**, 323 (1976).
[76]A. D. Buckingham and P. J. Stephens, Annu. Rev. Phys. Chem. **17**, 399 (1966).
[77]A. E. Neeves and M. H. Birnboim, J. Opt. Soc. Am. B **6**, 787 (1989).
[78]J. W. Haus, H. S. Zhou, S. Takami, M. Hirasawa, I. Honma, and H. Komiyama, J. Appl. Phys. **73**, 1043 (1993).
[79]H. S. Zhou, I. Honma, H. Komiyama, and J. W. Haus, Phys. Rev. B **50**, 12052 (1994).
[80]P. B. Johnson and R. W. Christy, Phys. Rev. B **9**, 5056 (1974).